Materials Today Advances 28 (2025) 100647

Contents lists available at ScienceDirect

Materials Today Advances

journal homepage: www.journals.elsevier.com/materials-today-advances/

MRI-activated magnetoelectric nanoparticles as theranostic agents

Martina Lenzuni [a,1], Denise Galante [b,1], Ilaria Faricelli [a,c], Serena Fiocchi [a], Emma Chiaramello [a], Cristina D'Arrigo [b], Roberta Tasso [d,e], Maria Chiara Ciferri [d,e], Rodolfo Quarto [d,e], Riccardo Marongiu [a], Roberta Resaz [e], Federico Zaottini [e,f], Riccardo Picasso [e], Carlo Martinoli [e,f], Paolo Ravazzani [a], Paolo Giannoni [d], Alessandra Marrella [a,*]

[a] Institute of Electronics, Computer and Telecommunication Engineering, Consiglio Nazionale Delle Ricerche (CNR-IEIIT), Genoa, Italy
[b] Institute of Chemical Sciences and Technologies "Giulio Natta", National Research Council of Italy (CNR-SCITEC), Genoa, Italy
[c] Department of Informatics, Bioengineering, Robotics and Systems Engineering (DIBRIS), University of Genoa, Genoa, Italy
[d] Department of Experimental Medicine (DIMES), University of Genoa, Genoa, Italy
[e] IRCCS Ospedale Policlinico San Martino, Genoa, Italy
[f] Department of Health Sciences (DISSAL), Radiology Section, University of Genoa, Genoa, Italy

ARTICLE INFO

Keywords:
Magnetoelectric nanoparticles
HT-29 cancer cells
High magnetic field
MRI
Multiphysics simulations
Magnetic field-mediated therapy

ABSTRACT

Magnetoelectric nanoparticles (MENPs) are gaining attention as wireless nanotools capable of converting magnetic fields into localized electric stimuli. However, their potential as theranostic agents is still in its infancy, and their responses under clinically relevant magnetic field conditions remain poorly understood. This study presents a systematic assessment of core-shell MENPs behavior on colorectal cancer cells, investigating their response under exposure to a clinical 3 T MRI scanner. After spontaneous internalization, MENP-treated and untreated cells were subjected to MRI fields, with morphological alterations and cell viability being assessed over time. A clear dose- and time-dependent cytotoxic effect was observed, with the highest level of cell death (>80 %) detected in the group treated with 100 μg/mL MENPs and exposed to MRI fields. These effects are likely associated with the interaction of the magnetic field with the nanoparticles, leading to localized electric field generation at the particle surface, which could disrupt cell membrane integrity and induce apoptosis-related pathways. Simulations of the MRI field distribution further supported the observed responses by providing a more comprehensive view of MRI-triggered MENP activation. Overall, the results here shown provide new insights for the establishment of MENPs-based theranostic platforms, which could affect cell viability while simultaneously enabling real-time imaging.

1. Introduction

In the rapidly evolving landscape of nanomedicine, magnetoelectric nanoparticles (MENPs) are emerging as wireless tools owing to their intrinsic magnetoelectric (ME) coupling, which enables the conversion of magnetic fields into localized electric stimuli and vice versa [1,2]. This bidirectional transduction is governed by the magnetoelectric coefficient, which quantifies the strength of the coupling and plays a crucial role in defining the efficacy of MENPs in biomedical applications, such as neuromodulation and drug release [3]. It has recently been hypothesized that MENPs could serve as theranostic agents, integrating a therapeutic action with real-time monitoring abilities [4]. This theranostic capability relies on the intrinsic properties of MENPs, which couple a magnetostrictive core and piezoelectric shell within a single nanostructure. In particular, when exposed to an external magnetic field, the magnetostrictive component in the core is subjected to a mechanical deformation, generating a strain that is transferred to the piezoelectric component, thereby producing an electric potential on the MENP shell [5]. This intrinsic magnetoelectric activity enables localized electrical stimulation in the surrounding environment without physical wiring or implanted electrodes, providing a minimally invasive therapeutic modality. At the same time, the magnetic cores of MENPs, typically composed of ferromagnetic materials such as cobalt ferrite ($CoFe_2O_4$), allow their detection via magnetic resonance imaging (MRI).

* Corresponding author.
E-mail address: alessandra.marrella@cnr.it (A. Marrella).
[1] These authors contributed equally to the work.

https://doi.org/10.1016/j.mtadv.2025.100647
Received 1 September 2025; Received in revised form 9 October 2025; Accepted 19 October 2025
Available online 22 October 2025

These nanoparticles generate local magnetic susceptibility differences with respect to the surrounding medium, creating small disturbances in the magnetic field. Such disturbances cause microscopic variations in proton precession frequency, which accelerate transverse magnetization dephasing and shorten T_2 relaxation times, resulting in signal hypointensities [6,7]. This interaction with MRI fields could enable real-time, non-invasive tracking of MENPs within biological tissue [8].

Importantly, the design of MENPs can be carefully tuned to optimize their performance in biomedical applications. For instance, increasing the size of the magnetic core while reducing the shell thickness has been reported to enhance the magnetoelectric coupling, maximizing strain transfer from the core to the shell and the resulting electric output [5]. Moreover, the composition, size, and morphology of both the magnetic core and the piezoelectric shell strongly influence the magnetoelectric coupling. In addition, the quality of the core–shell interface and the choice of particle geometry (e.g., nanospheres or nanorods) are crucial parameters to ensure effective strain transfer [3]. While cobalt ferrite ($CoFe_2O_4$) offers one of the highest saturation magnetization (Ms ~ 700 kA/m) and magnetostriction (~200 ppm) values among commonly used ferrites, alternative core materials such as magnetite (Fe_3O_4) or $CoMnFeO_4$ can be selected to modulate other properties, depending on the intended application [9,10]. Similarly, while barium titanate ($BaTiO_3$) is the most commonly employed piezoelectric shell due to its high piezoelectric coefficient, alternative piezoelectric materials such as bismuth ferrite ($BiFeO_3$) or lead zirconate titanate (PZT) can also be used to tune the coupling efficiency. In addition, other coatings such as gold, although not piezoelectric, can provide complementary functionalities including plasmonic effects, photothermal conversion, and improved biocompatibility, thereby enabling multimodal imaging and combined therapeutic approaches [11,12]. By carefully engineering both the core and shell properties, MENPs can be tailored for enhanced magnetoelectric response, controlled stimulation, targeted delivery, or simultaneous diagnostic and therapeutic applications.

Despite their promising potential, to date, only a few studies have explored the use of MENPs in conjunction with MRI, and none has systematically investigated the cellular-level interactions between MENPs and MRI fields. In particular, Kaushik et al. reported in 2019 a proof-of-concept study in which MRI (using a 3 T scanner) was employed to facilitate the delivery of MENPs into the brain of a baboon [8]. Similarly, in the work by Huang et al., MRI (a 3 T scanner) was used to monitor and target brain tumors in mice using drug-coated MENPs, which were engineered to cross the blood-brain barrier and provide magnetoelectricity-enhanced, glioma-targeted therapy [13]. However, a significant knowledge gap concerning the biological safety and efficacy of MENPs under clinical MRI conditions is still present. Importantly, although encouraging theoretical models and preliminary in vitro studies have been reported, the aforementioned studies employing clinically relevant magnetic fields remain primarily focused on targeting and imaging monitoring. As a result, the theranostic use of MENPs is not yet fully validated in clinical settings, which typically employ magnetic field strengths of 1.5 T or higher [14]. In particular, critical questions regarding the MENP distribution and the biological interaction of MENP-induced electric fields under MRI conditions remain unanswered. Clinical MRI systems generate complex electromagnetic environments that could be exploited to trigger MENP-mediated effects. Understanding how MENPs interact with these fields and how such interactions translate into cellular responses is pivotal for envisioning their future role in precision medicine. In recent state of the art regarding cancer therapy, MENPs have been primarily explored for their capability to locally deliver anticancer drugs [13,15–18]. Despite promising results in drug delivery applications, the intrinsic cytotoxic potential of MENPs and their field-induced interactions with cancer cells remain largely unexplored.

In this study, a systematic investigation of MENP-mediated effects was carried out on human colorectal carcinoma (HT-29) cells, chosen as a well-established model of epithelial tumors for evaluating MENP-cancer cell interactions under exposure to clinical (3 T) and preclinical (7 T) MRI conditions. These include static and time-varying magnetic fields that together constitute a complex electromagnetic environment capable of activating MENP-mediated effects. By integrating biological assays with advanced multiphysics modeling, the aim is to unravel the physical and biochemical phenomena driving MENP-cell interactions under magnetic field exposure. Both immediate and delayed cellular responses to MRI-triggered MENP activation were evaluated by assessing HT-29 cell viability and changes in cell morphology and adhesion immediately after exposure and following a 24-h recovery period, in order to capture transient as well as persistent effects. To distinguish the specific contributions of MENPs, MRI exposure, and their combination, appropriate control groups were included in the experimental design. Overall, this study provides new insights into the behavior of MENPs under clinical and preclinical diagnostic imaging settings, contributing to their rational design and potential application as theranostic agents.

2. Materials and methods

2.1. Materials and cell culture conditions

HT-29 cells were cultured in RPMI 1640 medium supplemented with 10 % Fetal Bovine Serum (FBS), 1 % L-Glutamine, and 1 % Penicillin/Streptomycin (all from Euroclone Spa, Pavia, Italy) and grown in standard conditions (37 °C, humidified incubator with 5 % CO_2). Magnetoelectric nanoparticles (MENPs) were purchased from Nanoshel UK Ltd. (Congleton, UK), with their characteristics being provided by the supplier. In particular, the nanoparticles feature a core composed of cobalt ferrite ($CoFe_2O_4$) with a diameter of 80–100 nm and a shell of barium titanate ($BaTiO_3$) with a thickness of 20–30 nm. The reported magnetoelectric coefficient was 4.3 mV cm^{-1} Oe^{-1}. Prior to use, MENPs were dispersed in a 0.25 M sodium citrate solution (adjusted to pH 7) and sonicated to enhance particle dispersion. Upon dilution in the culture medium for cell experiments, the final citrate concentration never exceeded 10 mM. Prior to any further application, the nanoparticles were sonicated again within a 40 kHz ultrasonic bath (ULTR-6L5, Labbox, Milan, Italy) for 15 min to ensure a timely homogeneous dispersion. Cell viability was assessed using the XTT cell viability assay (Cell Signaling Technology, Beverly, USA).

2.2. Evaluation of cell response to unstimulated MENPs

To evaluate the cellular response to MENPs in the absence of magnetic stimulation, both cell viability and time-lapse morphological changes were assessed by culturing cells with different MENP concentrations. In particular, HT-29 cells were seeded in standard 24-well plates and allowed to adhere overnight prior to treatment with MENPs at concentrations of 50, 100 and 250 μg/mL. Cell viability following 24 h of MENP exposure was assessed using the XTT assay according to the manufacturer's instructions. Absorbance was measured at 466 nm with background correction at 650 nm using a Spectra MR microplate reader (Dynex Technologies, Chantilly, VA, USA).

In parallel, a time-lapse analysis was conducted to monitor the early morphological responses of the MENPs-treated cells (100 μg/mL). To this aim, an Echo Revolution microscope (Echo, San Diego, USA) was utilized with a 20x 0.45 NA Olympus dry objective. The images were taken in a brightfield configuration, in light transmission mode. Two fields of view per well, each covering an area of 440 × 440 μm, were selected for the analysis to ensure representativeness of the overall cell population. The post-acquisition image analysis was performed manually utilizing the FIJI image analysis software [19]. Cell morphology was categorized as elongated, semi-elongated, or round depending on the aspect ratio (AR), calculated as the ratio between the major and minor axes of the cell (AR = major axis/minor axis). This classification was chosen to provide a more nuanced analysis of cell morphology, although

aspect ratio values can vary between different cell types [20–22]. In particular, round cells were defined as having an AR close to 1, representing a nearly perfect circular shape; semi-elongated cells, representing intermediate morphologies, were defined as having an AR between 1.2 and 2, capturing subtle deviations from roundness, and elongated cells were defined as having an AR greater than 2, corresponding to clearly stretched morphologies. Cells were counted manually, and for each of them, the corresponding shape descriptor was assessed. The same number of cells was evaluated at each time-point. The resulting numbers were translated to percentages to better compare different areas with different numbers of total cells, as the number in each field of view (FOV) varied between 150 and 270 cells. The percentage of cells in each morphological category was then quantified over time to assess their evolution.

2.3. MRI-responsive characterization of MENPs

To assess the MRI responsiveness of MENPs under clinical field conditions, a study was performed using 24-well plates. MENPs were suspended in RPMI solution supplemented with 10 % FBS at final concentrations of 0 (control), 50, and 100 μg/mL. For each concentration, 1 mL of the suspension was dispensed in triplicate into the wells. All MRI measurements were acquired on a Siemens 3 T scanner (Siemens Healthineers, Erlangen, Germany) equipped with a 64-channels head coil. The scanning protocol included a high resolution fat-suppressed turbo Spin-Echo Proton Density weighted sequence (TR 3300 ms; TE 26 ms; NEX 4; Slice thickness 2 mm; Matrix 0.9 × 0.9 mm; scan time 3 min and 50 s), a Gradient Echo FLASH 2D (TR 650 ms; TE 2,4 ms; NEX 4; Slice thickness 3 mm; Matrix 0.6 × 0.6 mm; scan time 5 min and 14 s), and a Susceptibility-Weighted sequence (TR 28 ms; TE 20,4 ms; NEX 5; Slice thickness 1 mm; Matrix 0.3 × 0.3 mm; scan time 5 min and 2 s). The sequences were repeated for a total scan time of 1 h. Quantitative T2* values were obtained by fitting the signal decay curves using a mono-exponential decay model in SyngoVia software (Siemens Healthineers, Erlangen, Germany). Regions of interest ($Ø = 0.5\ mm^2$) were placed at the center of each well to extract signal intensities. The relaxometric properties of the MENPs were then plotted as a function of nanoparticle concentration to assess their dose-dependent MRI contrast behavior. A detailed description of the pre-clinical MRI study performed at 7 T, with full scanning parameters, is available in the Supporting Information file.

2.4. Multiphysics simulations

To estimate the electric fields involved during MRI exposure, multiphysics models were developed and in silico studies were conducted. Specifically, the MRI system generates a static component of high intensity magnetic field (B0 = 3 T), plus a time-varying electromagnetic component of very small magnitude (B1 ~ 1.76 μT). As for the time-varying component generated by the RF coil, a model of the MRI system used in the experiment was created using the Sim4life Simulation platform (ZMT, Zurich, Switzerland, https://zmt.swiss/). In particular, a reference two-ports fed generic RF coil (12-rungs band-pass coil, diameter 350 mm, length 430 mm, 16 pF and 40.0 pF capacities in the end rings and rungs, respectively) tuned to 128 MHz was modelled according to the resonance frequency of typical 3 T RF head coils. The two 24-well cell culture plates were modelled with the same dimensions (length 127.5 mm, width 85.25 mm, height 22.5 mm, individual well diameter 16 mm, cell culture medium height 5 mm), material (polystyrene electric conductivity $\sigma = 0$ S/m $\varepsilon_r = 3.4$, cell culture medium $\sigma = 1.5$ S/m $\varepsilon_r = 69$) and positions as the corresponding experiment. Two separate broadband simulations for the two feed-ports placed 90° apart azimuthally on one end ring were performed, each yielding a linear B_1 polarization, which were then combined in postprocessing for obtaining a circularly polarized mode exposure. The computational domain was discretized using a non-uniform mesh with a maximum step of 10 x 10 × 10 mm, restricted to 1 x 1 × 1 mm in the volume of the two well plates.

At the nanoscale, an individual core-shell MENP was modelled in COMSOL Multiphysics® 6.1 as immersed in a fluid, simulating the surrounding culture medium. The 3D model represents a spherical MENP with a 90 nm diameter and a 25 nm shell thickness, implemented using an axisymmetric geometry. Material parameters, as well as the choice of physics and multiphysics couplings, were obtained from supplier datasheets, previous in silico studies on similar magnetoelectric nanoparticles, and are comprehensively summarized in Table S1 [5,23,24].

2.5. MRI exposure of cells in the presence of MENPs

2.5.1. Experimental design

A schematic overview of the experimental workflow is presented in Fig. 1. HT-29 cells were cultured under standard conditions and seeded at a density of ~2×10^5 cells/well into two 24-well plates (T0). After 24 h of incubation, the culture medium was replaced with fresh one containing MENPs at final concentrations of 0 (control), 50, and 100 μg/mL (T1). Culturing was performed for additional 24 h prior to MRI exposure (T2). One multiwell plate was placed inside a 3 T clinical MRI scanner and subjected to the mapping protocol (as described in paragraph 2.3) for a total exposure time of 60 min (MRI fields ON). Another multiwell plate was kept outside the MRI scanner and served as the "MRI field OFF" control. Following MRI exposure, cells were either immediately tested (T3) or returned to standard culture conditions and incubated for an additional 24 h before the analysis (T4).

2.5.2. Cell viability and morphological evaluation

Cell viability was evaluated using the XTT assay, as described in paragraph 2.2. Prior to the assay, wells were washed to remove any detached cells. At T4, non-adherent cells were collected by centrifugation and reseeded into new plates to determine whether the loss of adhesion was due to cell death events or a reversible loss of adhesion. In parallel, optical microscopy images were acquired using an Echo Revolution microscope to assess potential morphological changes. Control groups (0 μg/mL MENPs, with or without MRI field exposure) were used to assess the eventual impact of MRI fields on cell viability and morphology.

2.5.3. Flow cytometry analysis

To investigate the cell death pathways induced by MRI-activated MENPs, flow cytometry analysis was performed using the Annexin V-FITC/propidium iodide (PI) Apoptosis Detection Kit (BD Pharmigen, San Diego, USA), following the manufacturer's instructions. After treatment, both adherent and floating cells were collected to ensure inclusion of all potentially affected cell populations. Floating cells were first recovered from the culture supernatant by centrifugation (5 min at 300×*g*), while adherent cells were detached from the plastic support. Both populations were then combined, washed twice with cold PBS, and resuspended in 1 × binding buffer at a final concentration of 1×10^6 cells/mL for subsequent staining. Samples were acquired using a CytoFLEX S flow cytometer (Beckman Coulter, Brea, USA) and collected data were analyzed using the FlowJo_v 10.9.0 software. At least 10,000 events were acquired per sample. Based on Annexin V and PI staining, cells were classified as viable (Annexin V^-/PI^-), early apoptotic (Annexin V^+/PI^-), late apoptotic (Annexin V^+/PI^+), or necrotic (Annexin V^-/PI^+).

2.5.4. Immunofluorescence analysis

Immunostaining was conducted at the end of the experiments (T4) to examine the cell cytoskeletal responses to MENP exposure and MRI fields. Following previously established protocols [25,26], cells were fixed with 4 % paraformaldehyde in PBS (PFA; pH 7.4), permeabilized with 0.1 % Triton X-100, and blocked with 10 % goat serum solution in PBS to saturate unspecific binding sites. A mouse monoclonal *anti*-β Tubulin (Sigma T4026; Sigma-Aldrich, Milan, Italy) primary antibody was applied overnight at 4 °C (1:200, in 10 % goat serum/PBS), followed

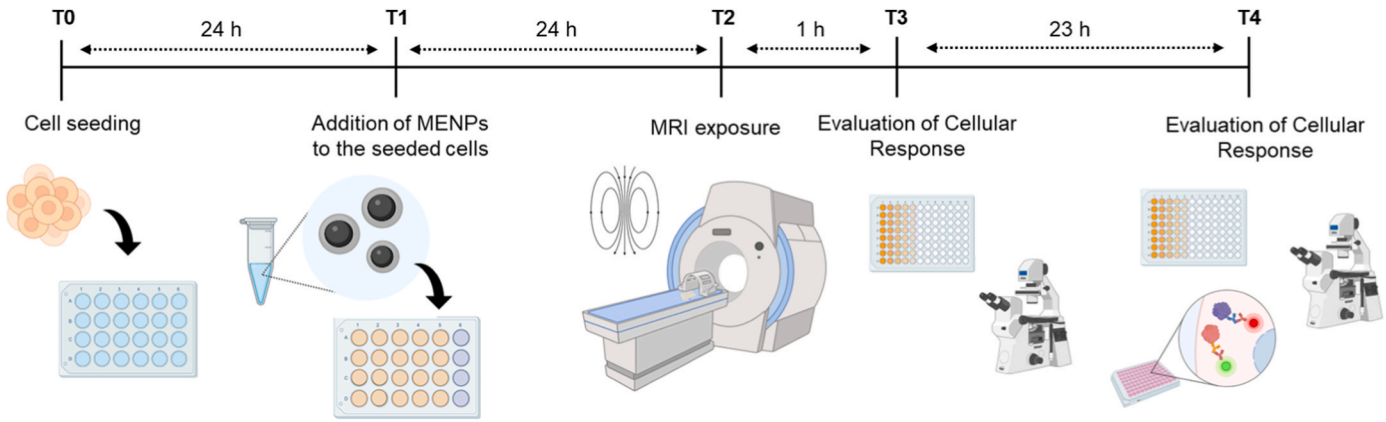

Fig. 1. Schematic representation of the experimental workflow. HT-29 cells were cultured and seeded into 24-well plates (T0). After 24 h, the culture medium was replaced with fresh medium containing MENPs at final concentrations of 0, 50, and 100 μg/mL (T1), followed by a 24-h incubation. Plates were then either exposed or not to clinical and pre-clinical MRI fields according to a T_2*-weighted imaging sequence (T2). Subsequently, cells were either immediately tested (T3) or cultured for an additional 24 h before the analysis (T4).

by 2 h incubation with an appropriate fluorescent secondary antibody (polyclonal goat anti-mouse Phycoerythrin-conjugated antibody; Dako Cytomation #R0480; Dako Cytomation A/S, Glostrup, Denmark; 1:200 in 10 % goat serum/PBS). Nuclei were counterstained with DAPI. Imaging was performed using an Echo Revolution microscope and analyzed with FIJI image analysis software. For quantitative analysis, β-tubulin fluorescence intensity was measured in the TRITC channel for each image and normalized to the corresponding DAPI signal to account for cell number [27,28]. Fluorescence values were expressed as relative β-tubulin intensity (%) compared to control cells not exposed to MRI fields. Cell morphology was analyzed as previously described in paragraph 2.2.

2.6. Statistical analysis

Data were analyzed using OriginPro 2023 (OriginLab, Northampton, United States) and GraphPad Prism 5 (GraphPad Software Inc., San Diego, USA). Statistical comparisons between different experimental groups were performed using Student's *t*-test. All data are expressed as mean ± standard deviation ($n \geq 3$), with a significance threshold set at $p < 0.05$ for statistical significance.

3. Results and discussion

3.1. Evaluation of MENPs cytotoxicity in the absence of MRI stimulation

HT-29 cells were incubated with increasing concentrations of MENPs (50, 100, and 250 μg/mL) for 24 h to evaluate their cytotoxicity. As shown in Fig. 2 (b), a concentration-dependent decrease in viability was observed. At 50 μg/mL, viability remained relatively high (84 ± 7 %), whereas a marked reduction was observed at 100 μg/mL, with viability decreasing to 54 ± 10 %. At the highest concentration tested (250 μg/mL), only 36 ± 1 % of cells remained viable. These findings align with previous studies on MENP cytotoxicity. For instance, Guduru et al. showed that 30 nm MENPs (50 μg/mL) did not significantly affect the viability of SKOV-3 ovarian cancer cells, maintaining around 95 % viability after 24 h (T3) without magnetic stimulation [29]. Similarly, Shotbolt et al. recently reported 80 % cell viability under the same conditions with 40 nm MENPs [30].

To investigate the dynamic interaction between MENPs and cancer cells, a time-lapse assay with optical microscopy was performed on HT-29 cells right after being in contact with MENPs (Fig. 2 (c–f)). While several studies have described the cytotoxic effects of MENPs, this represents, to the best of our knowledge, the first visualization of cellular morphological alterations induced by MENPs in real-time.

As shown in Fig. 2 (c), HT-29 cells treated with 100 μg/mL MENPs displayed progressive morphological changes within a few minutes: detachment and rounding were already evident at the first time point post-exposure, suggesting an acute cellular response to the nearby MENPs. Dashed boxes highlight the area where individual cells were tracked over time, revealing a characteristic sequence: slight cell shrinkage, detachment from the substrate, and rounding. Control cells subjected to the same time-lapse conditions but without MENP exposure showed no morphological changes over the 90-min period, confirming that the imaging conditions themselves did not induce stress in the cells.

Additionally, small dark aggregates of MENPs were observed within the cells, suggesting their internalization (Fig. 2 (c and d)). In this context, the electrostatic interactions between the MENPs and the cell membrane could lead to the displacement of the phosphate heads of the lipids, which are typically negatively charged, due to the repulsive forces [31]. This displacement can create transient pores in the cell membrane, facilitating the internalization of the MENPs even without the need for external stimuli, such as magnetic fields or active transport mechanisms. While previous studies have suggested that MENPs tend to spontaneously localize near the membrane of cancer cells due to the less charged surface of the cancer cell's membrane [4,15], the present findings evidence that these nanoparticles are not only attracted to the membrane but are also effectively internalized without external activation. This reveals a mechanism of passive cellular uptake, potentially driven by intrinsic electrostatic and dipolar interactions, enabling MENPs to exert intracellular effects even in the absence of magnetic stimulation. These results are in agreement with previous literature demonstrating that $BaTiO_3$ nanoparticles can be spontaneously internalized by cells [32,33]. Moreover, similar behavior has been observed for other types of nanoparticles coated with citrate, including iron oxide and gold nanoparticles, which have shown spontaneous cellular uptake despite their negative surface charge [34,35].

To further investigate the temporal progression of cellular fate following MENP exposure, time-lapse imaging was performed on HT-29 cells tracked in the dashed boxes of Fig. 2 (c). Starting at 120 min post-treatment with MENPs at the concentration of 100 μg/mL (Fig. 2 (d)), cells exhibited evident morphological signs of stress, including rounding and membrane blebbing. Over the following 60 min, these alterations intensified, culminating in a loss of membrane integrity and cellular fragmentation (Fig. 2 (d)).

To quantify such morphological change processes, cell morphology was classified into three categories according to the aspect ratio (AR), as depicted in Fig. 2 (e): elongated, semi-elongated, and round. The evolution of each category over the first 20 min is reported in Fig. 2 (f). Notably, over 60 % of cells adopted a round morphology by 5 min and

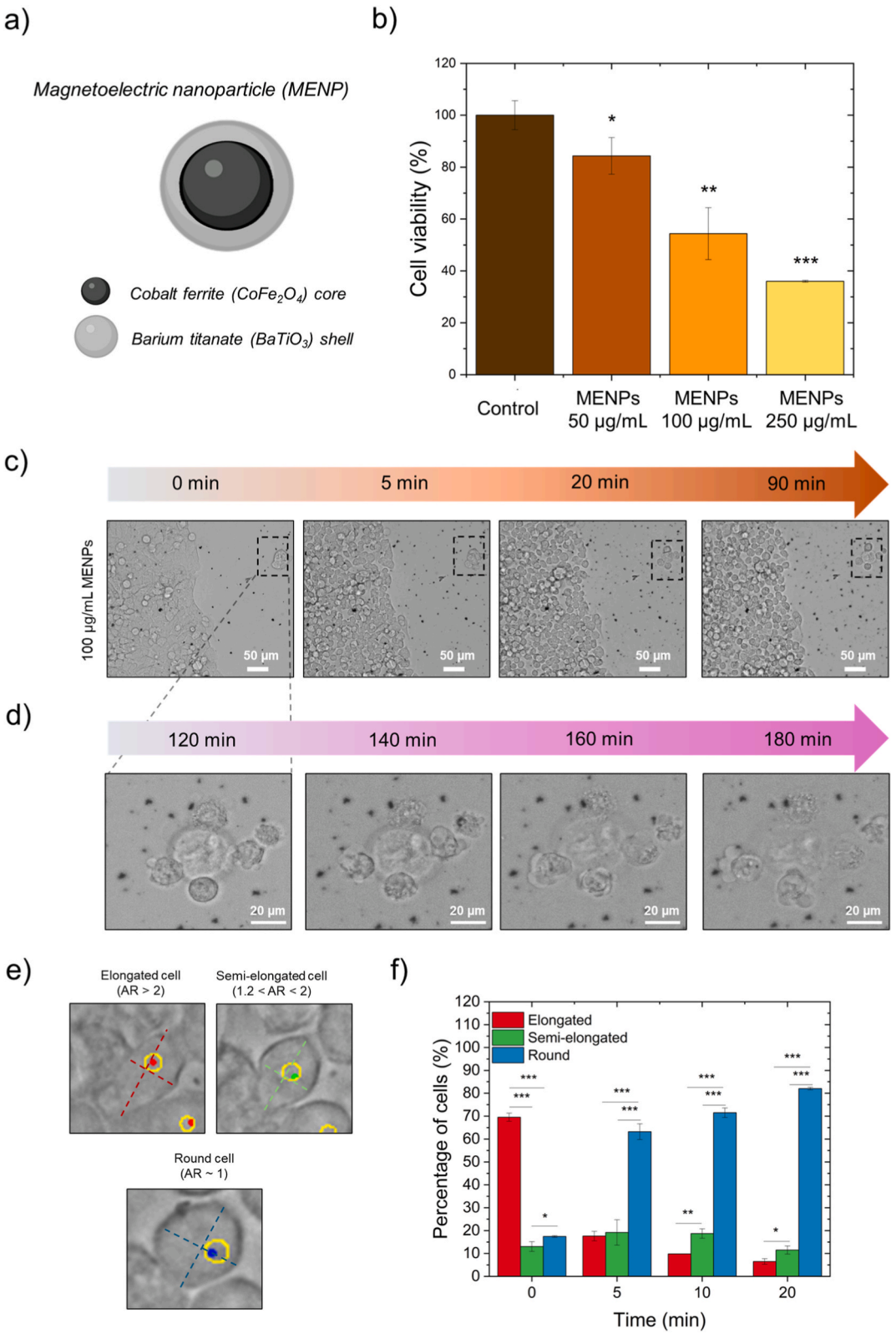

Fig. 2. Cellular response to unstimulated MENPs. a) Schematic representation of the core-shell MENP structure composed of a cobalt ferrite core and a barium titanate shell. b) Cell viability of HT-29 cells after 24 h of exposure to MENPs at concentrations of 50, 100 and 250 µg/mL, assessed via XTT assay. c) Time-lapse brightfield imaging analysis of cell morphology evolution over 90 min following MENP exposure. d) Representative zoomed-in images of the dashed area in c) highlighting apoptotic morphological changes induced by MENPs between 120 and 180 min post-exposure. e) Cell morphology was classified into three categories: elongated, semi-elongated and round. f) Quantitative analysis of the percentage of cells in each morphological class over time, with HT-29 cells treated with 100 µg/mL MENPs. Data are presented as mean ± standard deviation ($n \geq 3$). Statistical significance was evaluated using Student's t-test. *$p < 0.05$, **$p < 0.01$, ***$p < 0.001$.

over 80 % of cells by 20 min. The rapid morphological changes observed, such as increased cell roundness, suggest that MENPs, upon membrane attachment or internalization, induce cytoskeletal rearrangements in HT-29 cells. These fast responses may be mediated by intracellular signaling cascades, which rapidly reorganize the cytoskeleton, promote membrane blebbing, and trigger early apoptotic events. Similar morphological responses have been previously associated with apoptotic stress in HT-29 cells under different experimental conditions [36,37]. In addition, such rapid morphological alterations within the first minutes of exposure have also been reported for other cell types interacting with nanoparticles, including iron oxide-based nanomaterials, which were shown to induce cytoskeletal rearrangements and cell rounding shortly after contact [38,39], supporting the hypothesis that MENPs can immediately initiate apoptotic processes.

3.2. MRI responsiveness and multiphysics simulation of MENPs

The detection through MRI of $CoFe_2O_4$-$BaTiO_3$ core-shell MENPs was assessed through two independent phantom studies conducted using both a pre-clinical 7 T MRI scanner and a clinical 3 T system. T2*-weighted images were acquired confirming a dose-dependent signal reduction and supporting the suitability of MENPs as contrast agents across different field strengths (Fig. 3 (a, b) and Fig. S1).

In order to complement and interpret the experimental data, a multiphysics simulation model was developed to predict the magnetic and electric field distributions generated by the MRI scan on the samples. Fig. 3 (c, d) shows an example of the root-mean-square B1 field distribution and the resulting root-mean-square electric field distribution on a slice passing through the samples when the power in the two ports is adjusted so that the average B1 field within the volume occupied by the two well plates match the value provided by the realistic RF MRI coil software (i.e. 1.76 μT). Fig. 3 (e, f) shows more specifically the B1 and the resulting electric field distribution over the cell culture medium contained in the wells. B1 in the samples ranges between 1.08 and 3.96 μT, and the resulting electric field ranges between 0.6 and 31.4 V/m. In Fig. 3 (g), the single core–shell MENP is modelled as immersed in the surrounding culture medium. When subjected to the static magnetic field of 3 T, the magnetic core undergoes saturated magnetization, which induces a strong magnetostrictive response in the core, which in turn generates mechanical strain at the core–shell interface. The magnetostatic component, which is uniform throughout the volume inside the resonance bore, generates—via the magnetoelectric effect—a strong electric field at the nanoscale concentrated around the nanoparticle. The simulation results reveal electric field intensities exceeding 10^4 V/m near the shell–fluid interface. It can be noticed that, under MRI conditions, cell samples containing MENPs were exposed to a combination of electric fields resulting from both the MRI-generated electromagnetic fields (Fig. 3 (f)) and the magnetoelectric effects induced by the magnetically activated MENPs (Fig. 3 (h)). However, the electric field directly induced by the MRI radiofrequency component (B1 field) is extremely low (not exceeding a few tens of V/m) and is generally considered negligible with respect to any physiological cellular effect. In contrast, MENPs generate highly localized electric fields exceeding 10^4 V/m, which are orders of magnitude higher and potentially relevant for modulating cell behavior [40,41]. Importantly, these high localized electric fields may also induce a concomitant localized temperature increase due to Joule heating [24,42,43]. It should be noticed, however, that the present multiphysics model assumes a single isolated nanoparticle in a homogeneous medium. This idealized scenario neglects possible aggregation phenomena, heterogeneous cellular uptake, and the complex microenvironment found in vitro, which may significantly influence the effective distribution and magnitude of the induced electric fields.

3.3. Morphological impact of MENPs on HT-29 cells: pre- and post-MRI exposure analysis

To evaluate the potential impact of MRI exposure on HT-29 cells treated with MENPs, morphological analyses were conducted immediately before (T2) and right after (T3) the 1-h-long MRI scanning procedure (Fig. 4). At T2, control cells (without MENPs) and cells exposed to 50 μg/mL MENPs showed no significant morphological changes, while, with MENPs at 100 μg/mL, more pronounced morphological variations were detected immediately before MRI activation, as already shown in Fig. 2. Notably, at this stage, small aggregates of MENPs could be visualized as black dots within or in close proximity to the cells, suggesting that the nanoparticles may have already been internalized via passive mechanisms, as discussed in paragraph 3.1.

At T3 (i.e., following MRI exposure), a drastic change was observed only in the samples containing MENPs, for both concentrations analyzed: the overall number of cells significantly decreased, and the remaining cells exhibited a more pronounced rounded and contracted shape. This change was even more evident at 100 μg/mL MENPs, where only a few cells remained adherent, showing a small, spherical, and often fragmented or vacuolated morphology, typical of cell death [44]. These observations suggest that the combination of MENPs and MRI intensifies nanoparticle cytotoxic effects due to the unique MENPs magnetoelectric MRI-triggered activation. Specifically, when exposed to intense magnetic fields such as those used in MRI systems, MENPs can generate high localized electric fields (exceeding 10^4 V/m, Fig. 3 (h)), which could also lead to a localized temperature increase in their immediate proximity [23,24]. These magnetoelectric-induced effects are known to interfere with cellular function in multiple and potentially synergistic ways: the strong electric fields can disrupt transmembrane potential and interfere with ion channel activity or intracellular signaling pathways, while localized heating can enhance membrane permeability or denature essential intracellular molecules [45,46,47]. Moreover, activated MENPs can potentially contribute to the production of reactive oxygen species (ROS), leading to oxidative stress, mitochondrial dysfunction, and ultimately cell death [13].

3.4. Immediate and delayed response of HT-29 cells to MENPs and MRI exposure

3.4.1. Cell viability and morphology following MRI exposure

To further clarify the cellular response induced by MENPs under MRI conditions, the morphological analysis was extended to 24 h post-exposure (T4), after an initial assessment performed at T2 (pre-exposure) and then at T3 (immediately post-exposure). While earlier microscopy images highlighted initial morphological changes in HT-29 cells after treatment with MENPs and application of MRI fields, more evident effects emerged at later time points. As shown in Fig. 5 (a), optical microscopy images of HT-29 cells captured at T3 and T4 reveal distinct morphological responses depending on MENP concentration and MRI exposure. In the control groups (i.e., without MENPs), cells maintain a healthy and confluent monolayer at both time points, with no observable differences between samples exposed or not to MRI fields. This confirms that the MRI environment alone does not affect cell morphology or viability [48].

Upon treatment with 50 μg/mL MENPs in the absence of MRI fields, a slight reduction in cell density is noted at T3, along with some cells which assumed a temporary round morphology. However, this effect is not visible anymore at T4, indicating the absence of significant cytotoxicity and suggesting that transient responses may be triggered after MENP contact. In contrast, the exposure to MRI fields in the presence of 50 μg/mL MENPs leads to a more evident reduction in viable cells already at T3, confirming the results presented in Fig. 4. The cells appear sparser and fragmented, and this condition is further exacerbated at T4, when very few adherent cells are still visible.

At 100 μg/mL in the absence of MRI fields, cells exhibit signs of stress

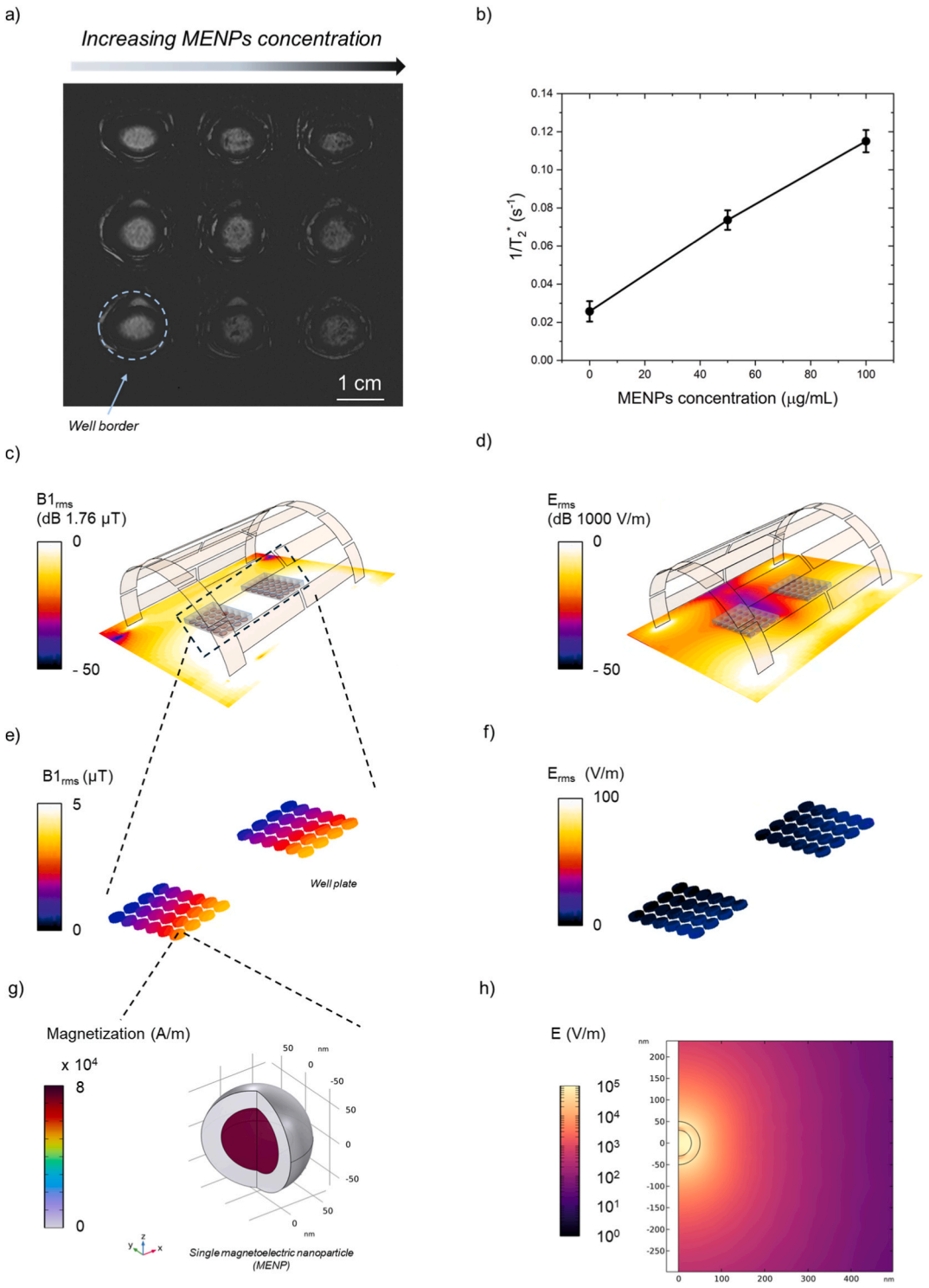

Fig. 3. MRI responsiveness and multiphysics simulation of MENPs with a 3T system. a) Susceptibility-Weighted MRI phantom images of well plates containing different concentrations of MENPs show the progressive decrease of signal intensity inside the well in function to increasing nanoparticle content. b) Quantification of relaxation rates ($1/T_2^*$) as a function of MENP concentration, confirming MRI responsiveness. Multiphysics simulations of the B1 field distribution (c, e) and the resulting electric field distribution (d, f) on a slice passing through the samples. Full domain simulations in (c) and (d) show the B1 field distribution and the corresponding electric field induced across the entire setup, including the RF coil (cage), structural supports, and the two well plates. The power at the two ports was adjusted so that the average B1 field within the region occupied by the plates matches the value provided by the realistic MRI coil model (1.76 μT). A zoomed-in view focusing on a single well plate is shown in (e) and (f), highlighting the spatial distribution of the B1 and the resulting electric field within the culture medium. In (g), the 3D simulation of a single core–shell MENP under a 3 T static magnetic field illustrates the magnetization of the core up to saturation. The resulting electric field distribution generated by the MENP is shown in (h), where a 2D slice reveals how the field extends into the surrounding medium.

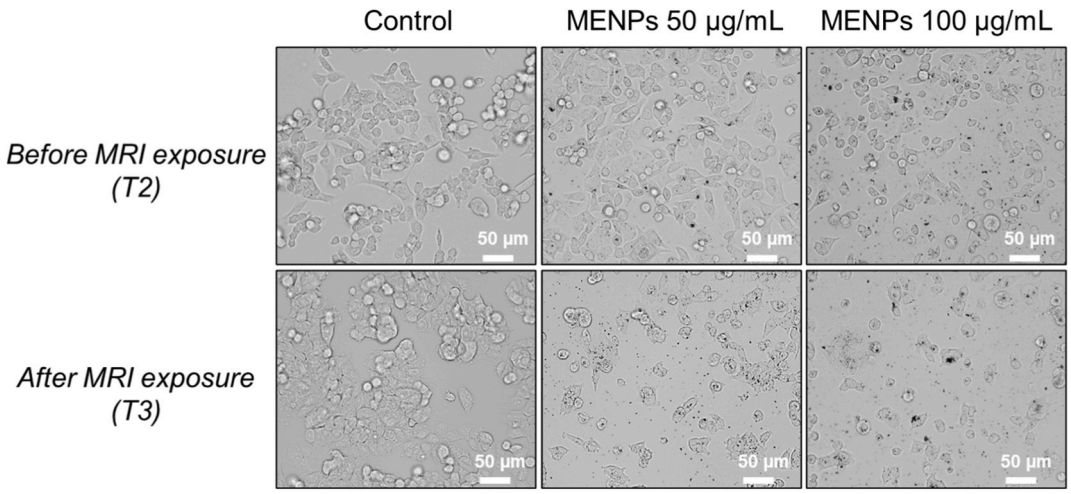

Fig. 4. Representative optical microscopy images of HT-29 cells incubated with MENPs at 0, 50, and 100 μg/mL concentrations, acquired immediately before (T2) and immediately after (T3) exposure to clinical MRI fields.

at T3 and T4, confirming previously shown data. However, when MRI fields are switched on, the MRI-triggered cytotoxic effect becomes more evident. Interestingly, after 1 day from MRI exposure (T4), this effect is even more emphasized with very few cells remaining attached to the culture plate. This indicates a synergistic interaction between high MENPs concentration and their magnetoelectric cytotoxic effect that severely compromises cell viability and adhesion. This enhanced effect may stem from the interaction between the MENPs and the magnetic fields, particularly when nanoparticles are internalized within the cells, as already anticipated in paragraph 3.3. The loss of cell adhesion observed also for the non-cytotoxic concentration (50 μg/mL) after MRI exposure indicates that MRI-activated MENPs may initiate apoptotic pathways, resulting in a slow and progressive cell death beyond the exposure period.

Under magnetic stimulation, MENPs generate very high electric fields (in the order of 10^5 V/m in the proximity of the shell) and, as a consequence, may induce localized temperature increases [24]. These mechanisms together can potentially act synergistically to compromise the integrity of lipid bilayers, thereby triggering signaling pathways associated with apoptosis and oxidative stress [49,50]. As also observed in Fig. 4, this process appears to begin with adhesion loss and evolves into cell death over time, particularly with higher MENP concentrations. The effects of these phenomena were clearly observed within the T4 (i.e., 24-h post-MRI exposure) time point, confirming that cell damage occurs as a combination of immediate physical effects and delayed biological responses, leading to progressive cell disruption following magnetoelectric activation (Fig. 5 (a)).

Quantitative viability assays (Fig. 5 (b and c)) confirmed these morphological trends. At T3, viability remained high in the 50 μg/mL MENP group without MRI exposure (90 ± 4 %) but dropped to 78 ± 4 % ($p < 0.01$) when MRI fields were applied, indicating an early cytotoxic effect triggered by the magnetic stimulation. In the 100 μg/mL group, viability was already significantly reduced regardless of MRI exposure (46 ± 4 % without MRI and 40 ± 5 % with MRI procedure), demonstrating a concentration-dependent effect. At T4, in the 50 μg/mL group, viability remained relatively stable without MRI (85 ± 6 %) but decreased markedly under MRI exposure (56 ± 11, $p < 0.01$). In the 100 μg/mL condition, only 39 ± 3 % of cells remained viable without MRI, whereas viability dropped to 17 ± 3 % when cells were exposed to MRI fields ($p < 0.001$), confirming that the MENPs cytotoxic effect could be enhanced by their MRI-triggered activation.

To better elucidate the cell death pathways activated in response to MENP treatment and MRI exposure, and specifically to distinguish between apoptotic (early vs late) and necrotic mechanisms, flow cytometry analysis was performed at T4 (24 h after MRI exposure). The results revealed a predominant activation of apoptotic processes in MENP-treated cells (Fig. S2). At 50 μg/mL, 46.2 ± 2.1 % of non-viable cells were in early apoptosis, 48.4 ± 2.0 % in late apoptosis, and only 5.4 ± 4.1 % underwent necrosis. At 100 μg/mL, the apoptotic response was even more pronounced, with 37.5 ± 1.3 % of cells in early apoptosis, 59.9 ± 1.6 % in late apoptosis, and only 2.7 ± 0.7 % in necrosis. These findings support the hypothesis that the observed cytotoxic effects are primarily mediated by apoptotic signaling rather than passive membrane rupture or necrotic pathways.

Complementary immunostaining analysis at T4 revealed a marked loss of tubulin signal and significant cytoskeletal rearrangement in HT-29 cells treated with MENPs and exposed to MRI fields (Fig. 6). This effect was particularly striking with 100 μg/mL MENPs, where β-tubulin availability in the cell cytoplasm appeared severely decreased, suggesting massive loss of essential cytoskeletal components and cytoskeletal reorganization. A diffuse red background signal, likely attributable to cellular debris released from damaged cells, can be observed in samples treated with 100 μg/mL MENPs, as also supported by the analysis of brightfield images (Fig. S3), which show membrane blebbing and progressive cell fragmentation characteristic of apoptosis. Correspondingly, morphometric analysis revealed a sharp increase in the proportion of round cells and a reduction in elongated morphologies under MRI conditions. Quantitative assessment of β-tubulin fluorescence intensity (Fig. S4) confirmed this observation, showing a 52.7 ± 11.7 % and 40.9 ± 6.6 % relative fluorescence for cells treated with 50 μg/mL and 100 μg/mL MENPs, respectively, under MRI fields compared to control cells not exposed to MRI fields, providing quantitative support for the observed cytoskeletal disruption. The observed alteration in β-tubulin signal intensity, along with the increased prevalence of rounded cell morphologies in MENP-treated cells exposed to MRI fields, is indicative of cytoskeletal disruption and β-tubulin depolymerization, as already reported by Hura et al. [51]. Similar phenomena have been reported in other studies involving nanoparticle-induced stress, where tubulin disassembly and cytoskeletal collapse were observed in response to TiO_2 and gold nanoparticles [52,53].

To further analyze the effects of the MRI magnetic fields, further tests were conducted by applying only the B0 field in the MRI system (Fig. S5). The results showed that, at T4, cells treated with 100 μg/mL MENPs and exposed to B0 field displayed 26 ± 1 % viability, which was significantly lower with respect to the samples not exposed to MRI fields ($p < 0.01$), but higher ($p < 0.01$) than the 17 ± 3 % viability observed when both the B0 and B1 components were activated in the MRI system. This notable reduction in cell viability under the B0 field only is

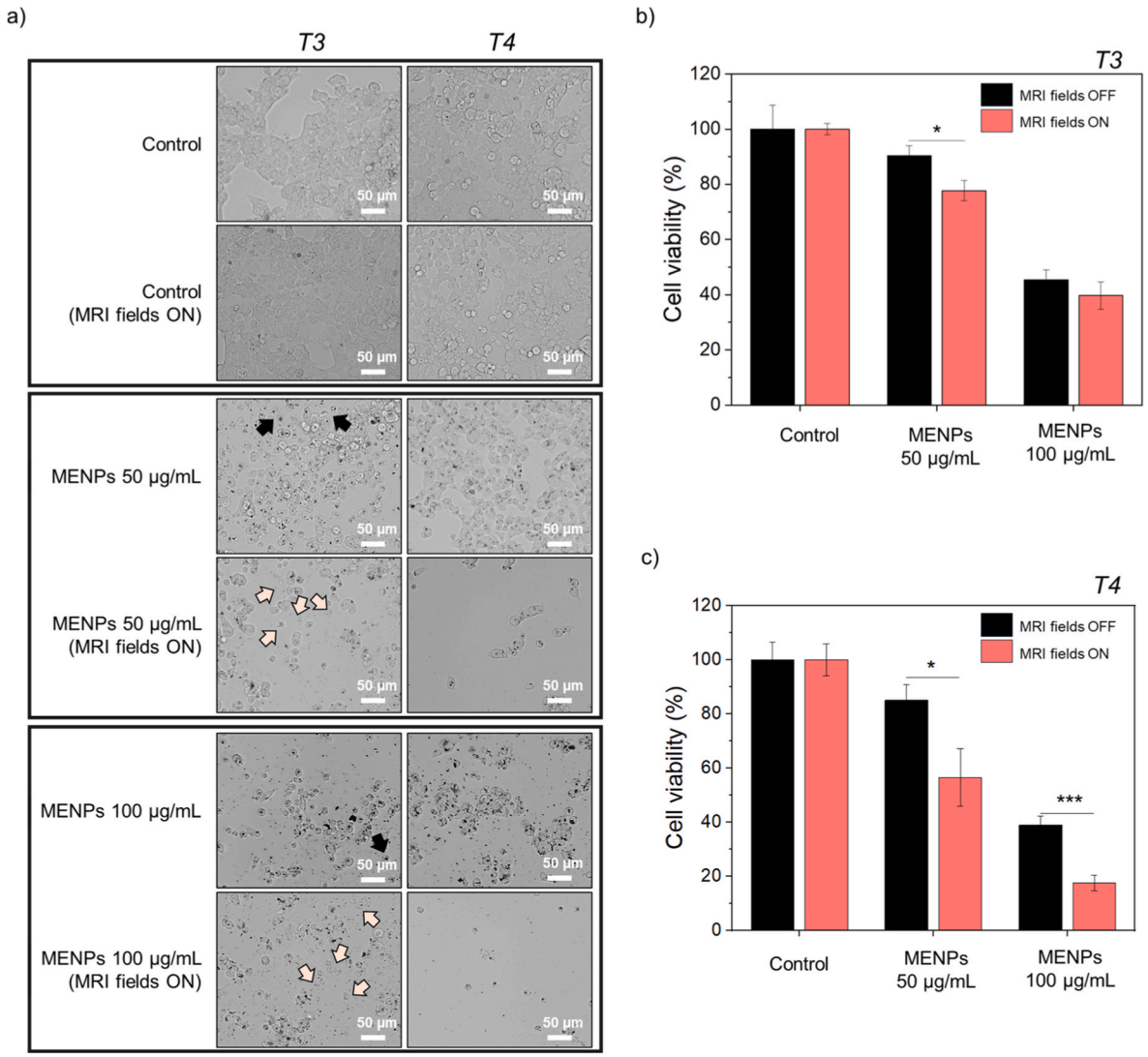

Fig. 5. Immediate and delayed response of HT-29 cells to MENPs and MRI exposure. a) Representative optical microscopy images of HT-29 cells incubated with or without MENPs (50 and 100 µg/mL), with and without MRI exposure, acquired immediately after MRI exposure (T3) and 24 h post-exposure (T4). Arrows indicate cells showing severe morphological damage, including loss of membrane integrity and signs of cell fragmentation. Cell viability of HT-29 cells assessed after incubation with MENPs at 50 and 100 µg/mL, with or without MRI exposure: b) viability measured immediately after MRI exposure (T3); c) viability measured 24 h post-exposure (T4). Black bars indicate samples not exposed to MRI fields (MRI fields OFF), while light red bars indicate samples exposed to MRI fields (MRI fields ON). Data are presented as mean ± standard deviation (n ≥ 3). Statistical significance was evaluated using Student's *t*-test. $^{*}p < 0.05$, $^{***}p < 0.001$. (For interpretation of the references to color in this figure legend, the reader is referred to the Web version of this article.)

primarily due to the localized electric field generated by the MENPs (Fig. 3(g)). As suggested by previous studies, additional contributions may arise from magnetic force-driven clustering of MENPs and altered cell mechanics, which can stress the cells and partially compromise membrane integrity [54,55]. When the alternating B1 field is activated, the cytotoxic effect becomes even more pronounced. The dynamic oscillation of the MENPs may generate a slight mechanical stress on the cells due to particle oscillation and a stronger local electric field that further disrupts cellular membranes. These results suggest that the combined effect of both magnetic fields (B0 + B1) activates a magnetoelectric response which is even more cytotoxic than exposure to the B0 field alone. At T3, no significant differences were observed between the B0 and B0 + B1 conditions, indicating that the effects of the combined magnetic fields become more pronounced over time. These results are in agreement with recent literature, which suggests that for MENP-based irreversible electroporation (IRE) processes, the application of a high DC magnetic field alone can induce the breakdown across the cancer cell membrane by delivering the energy required for IRE [4]. Notably, since the activation of the B1 field is essential to acquire MRI images (as shown in Fig. 3), its use is unavoidable in theranostic applications involving MENPs. Overall, the combination of higher MENP concentration and MRI exposure, as well as the presence of B0 + B1 fields, resulted in the most pronounced cytotoxicity. Therefore, the concurrent application of B0 and B1 fields not only enables imaging but also enhances the therapeutic impact of MENPs, supporting the rationale for their combined use.

3.4.2. *Reseeding of suspended cells*

To assess whether the non-adherent cells after 4 days of incubation from T4 (with and without MRI exposure) are completely dead or have initiated a damage process, the suspended cells were collected and reseeded in multiwell plates. After one day of reseeding (Fig. S6), no significant differences were observed among the treatment groups. As shown in Fig. 7, after 4 days of culture, cells in the control group were well-adhered to the substrate, regardless of the previous MRI exposure. These cells had successfully reattached and spread out, resembling a

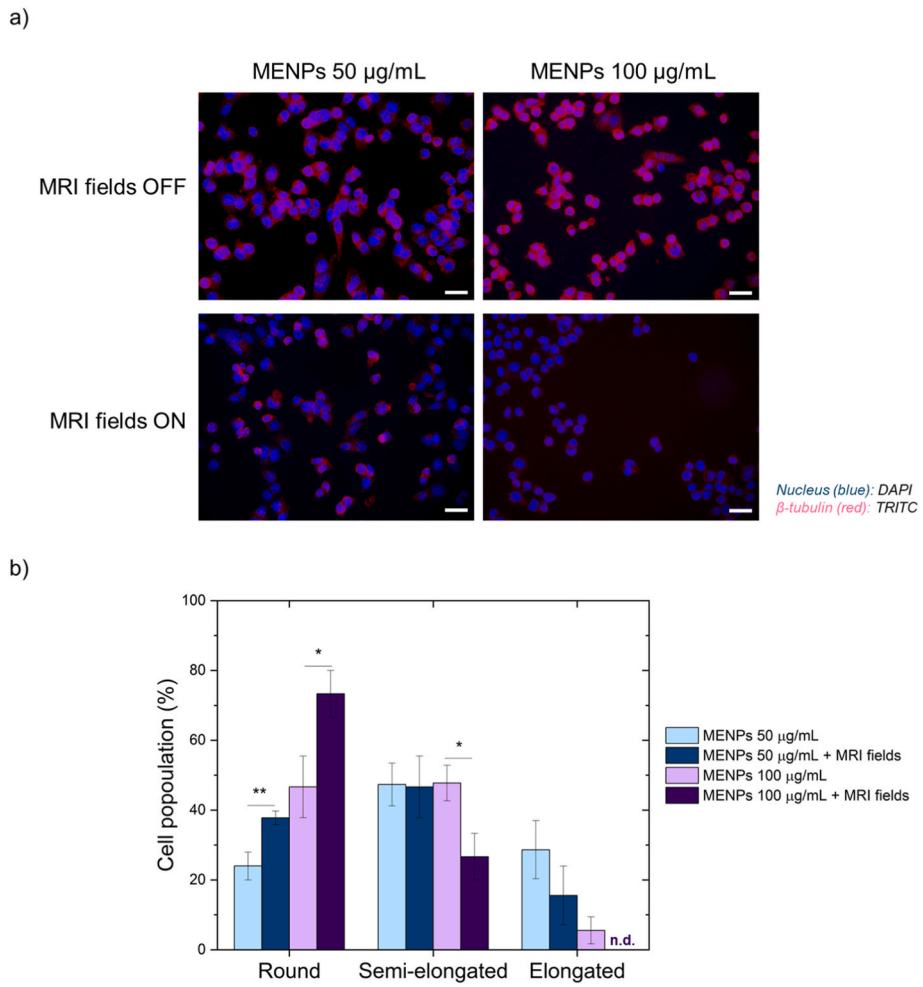

Fig. 6. Immunofluorescence staining and morphological analysis of HT-29 cells after MENP treatment and MRI exposure. a) Immunofluorescence images of HT-29 cells at 24 h post-exposure (T4), stained for β-tubulin (TRITC, red) and nuclei (DAPI, blue), following treatment with MENPs at 50 µg/mL and 100 µg/mL, with MRI fields ON or OFF. Scale bar = 10 µm. b) Quantification of cell shape distribution into round, semi-elongated, and elongated categories at 24 h post-exposure (T4). Data are presented as mean ± standard deviation (n ≥ 3), n. d., not detected. Statistical significance was evaluated using Student's *t*-test. $*p < 0.05$, $**p < 0.01$. (For interpretation of the references to color in this figure legend, the reader is referred to the Web version of this article.)

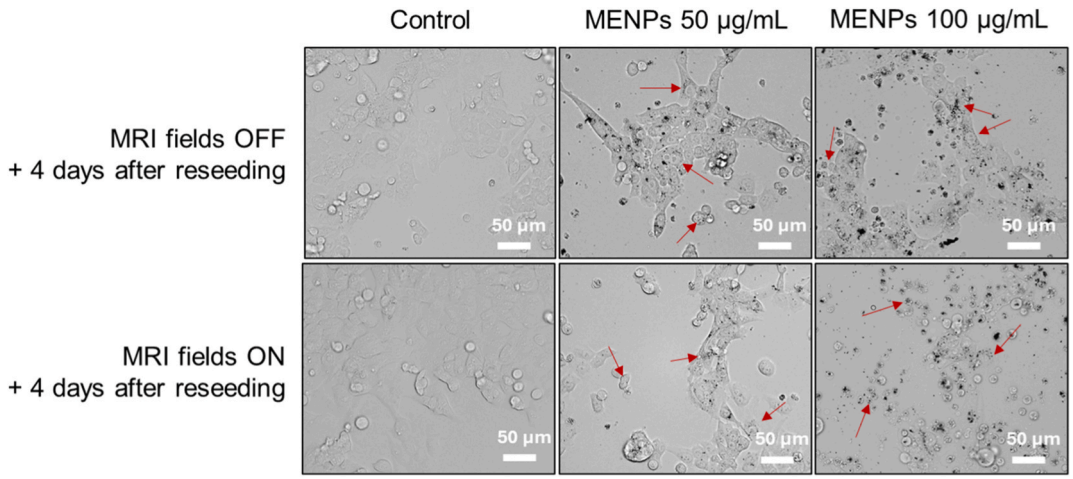

Fig. 7. Optical microscopy images of HT-29 suspended cells four days after being reseeded. Each image corresponds to a specific MENPs concentration and MRI exposure condition (MRI fields ON or MRI fields OFF) and illustrates whether non-adherent cells retained viability and were able to reattach to the well surface. Red arrows indicate representative examples of MENPs internalized by the cells. (For interpretation of the references to color in this figure legend, the reader is referred to the Web version of this article.)

typical, confluent monolayer. Cells treated with a lower MENPs concentration (50 μg/mL) exhibited healthy morphology, with the majority re-adhering to the substrate, although some cells remained rounded or damaged. In contrast, cells treated with 100 μg/mL MENPs and not exposed to MRI displayed a mixture of adherent cells, cells in suspension with altered morphology, and some cells showing signs of death. However, cells exposed to MRI fields under the same conditions showed almost no reattachment, with very few cells adhering to the substrate. Here, the reseeded cells containing MENPs, shown in Fig. 7, further support the hypothesis of spontaneous MENPs internalization, occurring independently of MRI field exposure. Indeed, MENPs are clearly detectable within most of the treated cells, both one (Fig. S6) and four days (Fig. 7) post-reseeding, while absent in untreated controls. Internalized MENPs could be observed in different subcellular locations, including near the plasma membrane, within the cytoplasm, and in proximity to the nuclear membrane.

Since most of these cells are overt apoptotic, as assessed by flow cytometry analysis, the MRI-triggered magnetoelectric cytotoxicity can be held responsible of cell damages that cannot be promptly repaired, persists in the long-term, and ultimately leads cells to programmed death cellular damage. In fact, cellular damage frequently initiates with the disturbance of adhesion mechanisms, which are essential for maintaining cell morphology, polarity, and communication. One of the early damage markers involves cytoskeletal architecture, such as the microtubule network, which plays a crucial role in organizing adhesion complexes and stabilizing cell shape. This phenomenon has been reported in various models of cellular stress and toxicity, where microtubule destabilization anticipates signs of cellular injury [56,57]. Therefore, the observed changes in β-tubulin organization (Fig. 6 (a)) as well as the proven non-viability of detached cells indicate that MRI fields trigger an initial stage of cellular damage and the subsequent breakdown of structural integrity.

To the best of available knowledge, this is the first report investigating the specific effects of MENPs on cell adhesion in the presence or absence of MRI fields, highlighting a novel concentration- and field-dependent impact on cellular integrity that has not been previously explored in the literature. These results confirm that the combined effect of high MENP concentration and MRI exposure significantly compromised the cells' capacity for stable reattachment and sustained proliferation.

4. Conclusions

In this work, a systematic investigation of core-shell magnetoelectric nanoparticles (MENPs) as magnetoelectrically responsive nanodevices for MRI-guided cancer therapy is provided, combining experimental and computational approaches to explore their MRI-triggered effects on HT-29 cancer cells. This is the first report to systematically assess the MENPs visualization under clinical and preclinical MRI systems as well as their MRI-triggered cytotoxicity, by means of time-lapse imaging, cell viability assays, together with an extensive in silico assessment to elucidate the magnetoelectric underlying mechanisms. First, it was demonstrated the potential of commercially available 3 T and 7 T systems to visualize even small concentrations of MENPs. In addition, MRI enabled to recognize different concentrations of MENPs in vitro through the quantification of signal decay on T2* sequences. These results open new perspectives for a potential use of MENPs as contrast agents for various applications, including identification of primitive tumors or metastases.

Then, it was proved that MENP exposure under MRI conditions leads to a boosted cytotoxic effect, inducing the disturbance of cell adhesion mechanisms, which is the first sign of cell damage. Notably, this study provides the first systematic investigation into the combined effects of MENPs and MRI magnetic fields (both static and alternating) on cell viability over extended time points, offering new insights into the synergistic mechanisms of magnetic field-induced toxicity, which have not been explored in such depth in prior research. While these results highlight the theranostic potential of MENPs, their translation to clinical practice will require a deeper understanding of long-term cytotoxicity, biodistribution and clearance routes, and possible immune responses. Importantly, future studies should also evaluate the effects of MENPs on healthy cells to ensure safe and selective application. In line with recent findings by Shotbolt et al., which demonstrated selective affinity of MENPs for malignant cells due to differences in electrical properties [58, 59], these investigations will help clarify MENP selectivity and safety in non-tumor cells.

All these findings open up significant opportunities for the use of magnetoelectric nanoparticles as theranostic agents. Their unique properties could potentially be harnessed by conjugating them with specific linkers to selectively target tumor cells or the extracellular matrix of tumor tissues. This would enable not only the selective damage of malignant tissues, but also their real-time visualization and detection. Such dual functionality paves the way for highly specific and minimally invasive approaches in cancer diagnosis and treatment.

CRediT authorship contribution statement

Martina Lenzuni: Writing – original draft, Visualization, Methodology, Investigation, Formal analysis. **Denise Galante:** Writing – review & editing, Methodology, Investigation. **Ilaria Faricelli:** Writing – review & editing, Investigation. **Serena Fiocchi:** Writing – review & editing, Visualization, Investigation. **Emma Chiaramello:** Writing – review & editing, Visualization, Investigation. **Cristina D'Arrigo:** Writing – review & editing, Methodology, Investigation. **Roberta Tasso:** Writing – review & editing, Methodology, Investigation. **Maria Chiara Ciferri:** Writing – review & editing, Methodology, Investigation. **Rodolfo Quarto:** Writing – review & editing, Validation, Supervision. **Riccardo Marongiu:** Writing – review & editing, Methodology, Investigation. **Roberta Resaz:** Writing – review & editing, Methodology, Investigation, Formal analysis. **Federico Zaottini:** Writing – review & editing, Methodology, Investigation, Formal analysis. **Riccardo Picasso:** Writing – review & editing, Methodology, Investigation, Formal analysis. **Carlo Martinoli:** Writing – review & editing, Supervision, Resources, Funding acquisition. **Paolo Ravazzani:** Writing – review & editing, Supervision, Resources, Funding acquisition. **Paolo Giannoni:** Writing – review & editing, Supervision, Resources, Methodology, Data curation. **Alessandra Marrella:** Writing – review & editing, Supervision, Project administration, Methodology, Data curation, Conceptualization.

Declaration of competing interest

The authors declare that they have no known competing financial interests or personal relationships that could have appeared to influence the work reported in this paper.

Acknowledgements

This work was partially supported by the Italian Ministry of Research, under the complementary actions of the NRRP "Fit4MedRob—Fit for Medical Robotics" grant (# PNC0000007).

Appendix A. Supplementary data

Supplementary data to this article can be found online at https://doi.org/10.1016/j.mtadv.2025.100647.

Data availability

Data will be made available on request.

References

[1] E. Hoque Apu, M. Nafiujjaman, S. Sandeep, A.V. Makela, A. Khaleghi, S. Vainio, C. H. Contag, J. Li, I. Balasingham, T. Kim, N. Ashammakhi, Biomedical applications of multifunctional magnetoelectric nanoparticles, Mater. Chem. Front. 6 (2022) 1368–1390, https://doi.org/10.1039/D2QM00093H.

[2] I.T. Smith, E. Zhang, Y.A. Yildirim, M.A. Campos, M. Abdel-Mottaleb, B. Yildirim, Z. Ramezani, V.L. Andre, A. Scott-Vandeusen, P. Liang, S. Khizroev, Nanomedicine and nanobiotechnology applications of magnetoelectric nanoparticles, WIREs Nanomedicine Nanobiotechnology 15 (2023) e1849, https://doi.org/10.1002/wnan.1849.

[3] M. Lenzuni, A. Marrella, E. Chiaramello, G. Suarato, P. Ravazzani, Exploring the bioengineering potential of $CoFe_2O_4$ -$BaTiO_3$ nanoparticles: a dive into the magnetoelectric coefficient, Adv. Electron. Mater. (2025) 2500014, https://doi.org/10.1002/aelm.202500014.

[4] V. Andre, M. Abdel-Mottaleb, M. Shotbolt, S. Chen, Z. Ramezini, E. Zhang, S. Conlan, O. Telisman, P. Liang, J.M. Bryant, R. Chomko, S. Khizroev, Foundational insights for theranostic applications of magnetoelectric nanoparticles, Nanoscale Horiz 10 (2025) 699–718, https://doi.org/10.1039/D4NH00560K.

[5] S. Fiocchi, E. Chiaramello, A. Marrella, G. Suarato, M. Bonato, M. Parazzini, P. Ravazzani, Modeling of core-shell magneto-electric nanoparticles for biomedical applications: effect of composition, dimension, and magnetic field features on magnetoelectric response, PLoS One 17 (2022) e0274676, https://doi.org/10.1371/journal.pone.0274676.

[6] Z. Mohammadi, N. Attaran, A. Sazgarnia, S.A.M. Shaegh, A. Montazerabadi, Superparamagnetic cobalt ferrite nanoparticles as T 2 contrast agent in MRI: in vitro study, IET Nanobiotechnol. 14 (2020) 396–404, https://doi.org/10.1049/iet-nbt.2019.0210.

[7] Z. Zhao, M. Li, J. Zeng, L. Huo, K. Liu, R. Wei, K. Ni, J. Gao, Recent advances in engineering iron oxide nanoparticles for effective magnetic resonance imaging, Bioact. Mater. 12 (2022) 214–245, https://doi.org/10.1016/j.bioactmat.2021.10.014.

[8] A. Kaushik, J. Rodriguez, D. Rothen, V. Bhardwaj, R.D. Jayant, P. Pattany, B. Fuentes, H. Chand, N. Kolishetti, N. El-Hage, K. Khalili, N.S. Kenyon, M. Nair, MRI-Guided, noninvasive delivery of magneto-electric drug nanocarriers to the brain in a nonhuman primate, ACS Appl. Bio Mater. 2 (2019) 4826–4836, https://doi.org/10.1021/acsabm.9b00592.

[9] T.M. Alfareed, Y. Slimani, M.A. Almessiere, S.E. Shirsath, M. Hassan, M. Nawaz, F. A. Khan, E.A. Al-Suhaimi, A. Baykal, Structure, magnetoelectric, and anticancer activities of core-shell Co0·8Mn0.2R0.02Fe1·98O4@BaTiO3 nanocomposites (R = Ce, Eu, Tb, Tm, or Gd), Ceram. Int. 48 (2022) 14640–14651, https://doi.org/10.1016/j.ceramint.2022.01.358.

[10] Y. Zhang, S. Chen, Z. Xiao, X. Liu, C. Wu, K. Wu, A. Liu, D. Wei, J. Sun, L. Zhou, H. Fan, Magnetoelectric nanoparticles incorporated biomimetic matrix for wireless electrical stimulation and nerve regeneration, Adv. Healthcare Mater. 10 (2021) 2100695, https://doi.org/10.1002/adhm.202100695.

[11] D. Kim, I. Efe, H. Torlakcik, A. Terzopoulou, A. Veciana, E. Siringil, F. Mushtaq, C. Franco, D. Von Arx, S. Sevim, J. Puigmartí-Luis, B. Nelson, N.A. Spaldin, C. Gattinoni, X. Chen, S. Pané, Magnetoelectric effect in hydrogen harvesting: magnetic field as a trigger of catalytic reactions, Adv. Mater. 34 (2022) 2110612, https://doi.org/10.1002/adma.202110612.

[12] A. Topete, A. Varela, M. Navarro-Real, R. Rial, A. Pardo, P. Taboada, Revisiting gold nanoshells as multifunctional biomedical nanotools, Coord. Chem. Rev. 523 (2025) 216250, https://doi.org/10.1016/j.ccr.2024.216250.

[13] Rong Huang, C. Lin, G. Jiang, M. Zhang, W. Gao, K. Aihemaiti, Q. Liu, J. Shi, W. Shi, Rongqin Huang, BBB-penetrating magnetoelectric nanoparticles with sustainable Gel formulation for enhanced chemotherapy and reduced postoperative glioma recurrence, Chem. Eng. J. 496 (2024) 154208, https://doi.org/10.1016/j.cej.2024.154208.

[14] M. van der Graaf, In vivo magnetic resonance spectroscopy: basic methodology and clinical applications, Eur. Biophys. J. 39 (2010) 527–540, https://doi.org/10.1007/s00249-009-0517-y.

[15] R. Guduru, P. Liang, C. Runowicz, M. Nair, V. Atluri, S. Khizroev, Magneto-electric nanoparticles to enable field-controlled high-specificity drug delivery to eradicate ovarian cancer cells, Sci. Rep. 3 (2013) 2953, https://doi.org/10.1038/srep02953.

[16] H. Mahdikia, F. Saadati, A.M. Alizadeh, S. Khalighfard, S. Bekeschus, B. Shokri, Low-frequency magnetic fields potentiate plasma-modified magneto-electric nanoparticle drug loading for anticancer activity in vitro and in vivo, Sci. Rep. 13 (2023) 17536, https://doi.org/10.1038/s41598-023-44683-6.

[17] A. Rodzinski, R. Guduru, P. Liang, A. Hadjikhani, T. Stewart, E. Stimphil, C. Runowicz, R. Cote, N. Altman, R. Datar, S. Khizroev, Targeted and controlled anticancer drug delivery and release with magnetoelectric nanoparticles, Sci. Rep. 6 (2016) 20867, https://doi.org/10.1038/srep20867.

[18] T.S. Stewart, A. Nagesetti, R. Guduru, P. Liang, E. Stimphil, A. Hadjikhani, L. Salgueiro, J. Horstmyer, R. Cai, A. Schally, S. Khizroev, Magnetoelectric nanoparticles for delivery of antitumor peptides into glioblastoma cells by magnetic fields, Nanomed 13 (2018) 423–438, https://doi.org/10.2217/nnm-2017-0300.

[19] J. Schindelin, I. Arganda-Carreras, E. Frise, V. Kaynig, M. Longair, T. Pietzsch, S. Preibisch, C. Rueden, S. Saalfeld, B. Schmid, J.-Y. Tinevez, D.J. White, V. Hartenstein, K. Eliceiri, P. Tomancak, A. Cardona, Fiji: an open-source platform for biological-image analysis, Nat. Methods 9 (2012) 676–682, https://doi.org/10.1038/nmeth.2019.

[20] A.A. Alobaidi, B. Sun, Probing three-dimensional collective cancer invasion with DIGME, Cancer Converg 1 (2017) 1, https://doi.org/10.1186/s41236-017-0004-9.

[21] J. Kim, Y. Cao, C. Eddy, Y. Deng, H. Levine, W.-J. Rappel, B. Sun, The mechanics and dynamics of cancer cells sensing noisy 3D contact guidance, Proc. Natl. Acad. Sci. 118 (2021) e2024780118, https://doi.org/10.1073/pnas.2024780118.

[22] C. Luna, A.G. Yew, A.H. Hsieh, Effects of angular frequency during clinorotation on mesenchymal stem cell morphology and migration, Npj Microgravity 1 (2015) 15007, https://doi.org/10.1038/npjmgrav.2015.7.

[23] M. Lenzuni, P. Giannoni, E. Chiaramello, S. Fiocchi, G. Suarato, P. Ravazzani, A. Marrella, Multiphysics analysis of the dual role of magnetoelectric nanoparticles in a microvascular environment: from magnetic targeting to electrical activation, Front. Bioeng. Biotechnol. 12 (2025) 1467328, https://doi.org/10.3389/fbioe.2024.1467328.

[24] A. Marrella, P. Giannoni, M. Lenzuni, G. Suarato, S. Fiocchi, E. Chiaramello, P. Ravazzani, Temperature-dependent cytokine neutralization induced by magnetoelectric nanoparticles: an in silico study, Int. J. Mol. Sci. 25 (2024) 13591, https://doi.org/10.3390/ijms252413591.

[25] P. Giannoni, M. Grosso, G. Fugazza, M. Nizzari, M.C. Capra, R. Bianchi, R. Fiocca, S. Salvi, F. Montecucco, M. Bertolotto, F. Fais, M. Salio, E. Barisione, D. de Totero, Establishment and characterization of a novel fibroblastic cell line (SCI13D) derived from the broncho-alveolar lavage of a patient with fibrotic hypersensitivity pneumonitis, Biomedicines 9 (2021), https://doi.org/10.3390/biomedicines9091193.

[26] A. Marrella, P. Giannoni, I. Pulsoni, R. Quarto, R. Raiteri, S. Scaglione, Topographical features of graphene-oxide-functionalized substrates modulate cancer and healthy cell adhesion based on the cell tissue of origin, ACS Appl. Mater. Interfaces 10 (2018) 41978–41985, https://doi.org/10.1021/acsami.8b15036.

[27] S. Challa, K.W. Ryu, A.L. Whitaker, J.C. Abshier, C.V. Camacho, W.L. Kraus, Development and characterization of new tools for detecting poly(ADP-ribose) in vitro and in vivo, eLife 11 (2022) e72464, https://doi.org/10.7554/eLife.72464.

[28] Q. Ma, J.R. Beal, A. Bhurke, A. Kannan, J. Yu, R.N. Taylor, I.C. Bagchi, M. K. Bagchi, Extracellular vesicles secreted by human uterine stromal cells regulate decidualization, angiogenesis, and trophoblast differentiation, Proc. Natl. Acad. Sci. 119 (2022) e2200252119, https://doi.org/10.1073/pnas.2200252119.

[29] R. Guduru, S. Khizroev, Magnetic field-controlled release of paclitaxel drug from functionalized magnetoelectric nanoparticles, Part. Part. Syst. Char. 31 (2014) 605–611, https://doi.org/10.1002/ppsc.201300238.

[30] M. Shotbolt, E. Zhu, V. Andre, E. Zhang, I. Duran, J. Bryant, W. El-Rifai, P. Liang, S. Khizroev, Catalytic degradation of organic dyes indicates anti-proliferative effects of magnetoelectric nanoparticles, J. Electron. Mater. (2025), https://doi.org/10.1007/s11664-025-11843-5.

[31] S. Betal, M. Dutta, B. Shrestha, L. Cotica, L. Tang, A. Bhalla, R. Guo, Cell permeation using core-shell magnetoelectric nanoparticles, Integrated Ferroelectrics Int. J. 174 (2016) 186–194, https://doi.org/10.1080/10584587.2016.1196332.

[32] C. Dempsey, I. Lee, K.R. Cowan, J. Suh, Coating barium titanate nanoparticles with polyethylenimine improves cellular uptake and allows for coupled imaging and gene delivery, Colloids Surf. B Biointerfaces 112 (2013) 108–112, https://doi.org/10.1016/j.colsurfb.2013.07.045.

[33] O. Matar, O.M. Posada, N.S. Hondow, C. Wälti, M. Saunders, C.A. Murray, R.M. D. Brydson, S.J. Milne, A.P. Brown, Barium titanate nanoparticles for biomarker applications, J. Phys. Conf. Ser. 644 (2015) 012037, https://doi.org/10.1088/1742-6596/644/1/012037.

[34] C. Freese, C. Uboldi, M.I. Gibson, R.E. Unger, B.B. Weksler, I.A. Romero, P.-O. Couraud, C.J. Kirkpatrick, Uptake and cytotoxicity of citrate-coated gold nanospheres: comparative studies on human endothelial and epithelial cells, Part. Fibre Toxicol. 9 (2012) 23, https://doi.org/10.1186/1743-8977-9-23.

[35] M. Safi, J. Courtois, M. Seigneuret, H. Conjeaud, J.-F. Berret, The effects of aggregation and protein corona on the cellular internalization of iron oxide nanoparticles, Biomaterials 32 (2011) 9353–9363, https://doi.org/10.1016/j.biomaterials.2011.08.048.

[36] B.P.L. Liu, E.Y.Y. Chong, F.W.K. Cheung, J.-A. Duan, C.-T. Che, W.K. Liu, Tangutorine induces p21 expression and abnormal mitosis in human colon cancer HT-29 cells, Biochem. Pharmacol. 70 (2005) 287–299, https://doi.org/10.1016/j.bcp.2005.04.024.

[37] K. Thangaraj, B. Balasubramanian, S. Park, K. Natesan, W. Liu, V. Manju, Orientin induces G0/G1 cell cycle arrest and mitochondria mediated intrinsic apoptosis in human colorectal carcinoma HT29 cells, Biomolecules 9 (2019) 418–425, https://doi.org/10.3390/biom9090418.

[38] A. Colin, L. Bonnemay, C. Gayrard, J. Gautier, Z. Gueroui, Triggering signaling pathways using F-actin self-organization, Sci. Rep. 6 (2016) 34657, https://doi.org/10.1038/srep34657.

[39] J.E. Perez, F. Fage, D. Pereira, A. Abou-Hassan, S. Asnacios, A. Asnacios, C. Wilhelm, Transient cell stiffening triggered by magnetic nanoparticle exposure, J. Nanobiotechnol. 19 (2021) 117, https://doi.org/10.1186/s12951-021-00790-y.

[40] S. Kopyl, R. Surmenev, M. Surmeneva, Y. Fetisov, A. Kholkin, Magnetoelectric effect: principles and applications in biology and medicine—a review, Mater. Today 12 (2021), https://doi.org/10.1016/j.mtbio.2021.100149.

[41] A. Marrella, G. Suarato, S. Fiocchi, E. Chiaramello, M. Bonato, M. Parazzini, P. Ravazzani, Magnetoelectric nanoparticles shape modulates their electrical output, Front. Bioeng. Biotechnol. 11 (2023) 1219777, https://doi.org/10.3389/fbioe.2023.1219777.

[42] F. Guo, X. Nie, J. Hong, Yapeng Zhang, J. Sun, Yu Zhang, Influence of joule heating during single-cell electroporation simulation under IRE and H-FIRE pulses, Mater. Today Commun. 36 (2023) 106853, https://doi.org/10.1016/j.mtcomm.2023.106853.

[43] U. Pliquett, Joule heating during solid tissue electroporation, Med. Biol. Eng. Comput. 41 (2003) 215–219, https://doi.org/10.1007/BF02344892.
[44] L. Harmse, N. Dahan-Farkas, J.-L. Panayides, W. van Otterlo, C. Penny, Aberrant apoptotic response of colorectal cancer cells to novel nucleoside analogues, PLoS One 10 (2015) e0138607, https://doi.org/10.1371/journal.pone.0138607.
[45] M.P. Stewart, R. Langer, K.F. Jensen, Intracellular delivery by membrane disruption: mechanisms, strategies, and concepts, Chem. Rev. 118 (2018) 7409–7531, https://doi.org/10.1021/acs.chemrev.7b00678.
[46] M. Delcea, N. Sternberg, A.M. Yashchenok, R. Georgieva, H. Bäumler, H. Möhwald, A.G. Skirtach, Nanoplasmonics for dual-molecule release through nanopores in the membrane of red blood cells, ACS Nano 6 (2012) 4169–4180, https://doi.org/10.1021/nn3006619.
[47] L.-L. Tang, C.X. Sun, H. Liu, Y. Mi, C.-G. Yao, C.-X. Li, Steep pulsed electric fields modulate cell apoptosis through the change of intracellular calcium concentration, Colloids Surf. B Biointerfaces 57 (2007) 209–214, https://doi.org/10.1016/j.colsurfb.2007.02.008.
[48] J. Miyakoshi, Effects of static magnetic fields at the cellular level, Eff. Static Magn. Fields Relev. Hum. Health 87 (2005) 213–223, https://doi.org/10.1016/j.pbiomolbio.2004.08.008.
[49] W.E. Ford, W. Ren, P.F. Blackmore, K.H. Schoenbach, S.J. Beebe, Nanosecond pulsed electric fields stimulate apoptosis without release of pro-apoptotic factors from mitochondria in B16f10 melanoma, Arch. Biochem. Biophys. 497 (2010) 82–89, https://doi.org/10.1016/j.abb.2010.03.008.
[50] C.M. Worsley, R.B. Veale, E.S. Mayne, Inducing apoptosis using chemical treatment and acidic pH, and detecting it using the annexin V flow cytometric assay, PLoS One 17 (2022) e0270599, https://doi.org/10.1371/journal.pone.0270599.
[51] N. Hura, A. Naaz, S.S. Prassanawar, S.K. Guchhait, D. Panda, Drug-clinical agent molecular hybrid: synthesis of diaryl(trifluoromethyl)pyrazoles as tubulin targeting anticancer agents, ACS Omega 3 (2018) 1955–1969, https://doi.org/10.1021/acsomega.7b01784.
[52] D. Choudhury, P.L. Xavier, K. Chaudhari, R. John, A.K. Dasgupta, T. Pradeep, G. Chakrabarti, Unprecedented inhibition of tubulin polymerization directed by gold nanoparticles inducing cell cycle arrest and apoptosis, Nanoscale 5 (2013) 4476–4489, https://doi.org/10.1039/C3NR33891F.
[53] Z. Mao, B. Xu, X. Ji, K. Zhou, X. Zhang, M. Chen, X. Han, Q. Tang, X. Wang, Y. Xia, Titanium dioxide nanoparticles alter cellular morphology via disturbing the microtubule dynamics, Nanoscale 7 (2015) 8466–8475, https://doi.org/10.1039/C5NR01448D.
[54] J. Beltran-Huarac, D.N. Yamaleyeva, G. Dotti, S. Hingtgen, M. Sokolsky-Papkov, A. V. Kabanov, Magnetic control of protein expression via magneto-mechanical actuation of ND-PEGylated iron oxide nanocubes for cell therapy, ACS Appl. Mater. Interfaces 15 (2023) 19877–19891, https://doi.org/10.1021/acsami.3c00179.
[55] Y. Quan, Z. Huang, Y. Wang, Y. Liu, S. Ding, Q. Zhao, X. Chen, H. Li, Z. Tang, B. Zhou, Y. Zhou, Coupling of static ultramicromagnetic field with elastic micropillar-structured substrate for cell response, Mater. Today Bio 23 (2023) 100831, https://doi.org/10.1016/j.mtbio.2023.100831.
[56] J.V. Small, B. Geiger, I. Kaverina, A. Bershadsky, How do microtubules guide migrating cells? Nat. Rev. Mol. Cell Biol. 3 (2002) 957–964, https://doi.org/10.1038/nrm971.
[57] K.M. Yamada, B. Geiger, Molecular interactions in cell adhesion complexes, Curr. Opin. Cell Biol. 9 (1997) 76–85, https://doi.org/10.1016/S0955-0674(97)80155-X.
[58] M. Shotbolt, J. Bryant, P. Liang, S. Khizroev, Mechanism and applications of magnetoelectric nanoparticles in cancer therapy, Nanomed (2025) 1–13, https://doi.org/10.1080/17435889.2025.2545746.
[59] M. Shotbolt, J. Bryant, P. Liang, S. Khizroev, Physics of selective targeting of cancer cells by magnetoelectric nanoparticles: exploring the role of conductivity and capacitance in tumor-specific attraction, Adv. Theory Simul. 2025 (2025) e00739, https://doi.org/10.1002/adts.202500739.